nature chemistry

REVIEW ARTICLE

PUBLISHED ONLINE: 20 MARCH 2013 | DOI: 10.1038/NCHEM.1589

The chemistry of two-dimensional layered transition metal dichalcogenide nanosheets

Manish Chhowalla[1*], Hyeon Suk Shin[2], Goki Eda[3,4,5], Lain-Jong Li[6], Kian Ping Loh[4,5] and Hua Zhang[7]

Ultrathin two-dimensional nanosheets of layered transition metal dichalcogenides (TMDs) are fundamentally and technologically intriguing. In contrast to the graphene sheet, they are chemically versatile. Mono- or few-layered TMDs — obtained either through exfoliation of bulk materials or bottom-up syntheses — are direct-gap semiconductors whose bandgap energy, as well as carrier type (n- or p-type), varies between compounds depending on their composition, structure and dimensionality. In this Review, we describe how the tunable electronic structure of TMDs makes them attractive for a variety of applications. They have been investigated as chemically active electrocatalysts for hydrogen evolution and hydrosulfurization, as well as electrically active materials in opto-electronics. Their morphologies and properties are also useful for energy storage applications such as electrodes for Li-ion batteries and supercapacitors.

Recent research has shown that in addition to the composition and arrangement of atoms in materials, dimensionality plays a crucial role in determining their fundamental properties. This has been most strikingly highlighted over the past few years with two-dimensional (2D) graphene, which exhibits exotic condensed-matter phenomena that are absent in bulk graphite[1–3]. The rapid pace of progress in graphene and the methodology developed in preparing ultrathin layers has led to exploration of other 2D materials[4–17]. In particular, single layers of transition metal dichalcogenides (TMDs) with lamellar structures similar to that of graphite have received significant attention because some of them are semiconductors with sizable bandgaps and are naturally abundant[5,6].

Graphene, while being fundamentally and technologically interesting for a variety of applications, is chemically inert and can only be made active by functionalization with desired molecules[18], which in turn results in the loss of some of its exotic properties. In contrast, single-layered 2D TMDs — whose generalized formula is MX_2, where M is a transition metal of groups 4–10 and X is a chalcogen (Fig. 1) — exhibit versatile chemistry. This offers opportunities for fundamental and technological research in a variety of fields including catalysis, energy storage, sensing and electronic devices such as field-effect transistors and logic circuits.

The properties of bulk TMDs are diverse — ranging from insulators such as HfS_2, semiconductors such as MoS_2 and WS_2, semimetals such as WTe_2 and $TiSe_2$, to true metals such as NbS_2 and VSe_2. A few bulk TMDs such as $NbSe_2$ and TaS_2 exhibit low-temperature phenomena including superconductivity, charge density wave (CDW, a periodic distortion of the crystal lattice) and Mott transition (metal to non-metal transition)[19–21]. Exfoliation of these materials into mono- or few-layers largely preserves their properties, and also leads to additional characteristics due to confinement effects[7–9]. The chemistry of MX_2 compounds thus offers opportunities for going beyond graphene and opening up new fundamental and technological pathways for inorganic 2D materials.

In this Review, we highlight some interesting properties of monolayered TMDs and how they are influenced by their constituent elements. Some recent progress on their synthesis, based on chemical vapour deposition (CVD) and chemical exfoliation of the bulk materials, is reviewed along with the implementation of the resulting 2D materials as electrodes in energy storage devices, electrocatalysts for the hydrogen evolution reaction, and as high-performance materials for flexible opto-electronics devices.

Composition, crystal phases and electronic structure

Many TMDs crystallize in a graphite-like layered structure that leads to strong anisotropy in their electrical, chemical, mechanical and thermal properties[22]. Group 4–7 TMDs in Fig. 1a are predominantly layered, whereas some of group 8–10 TMDs are commonly found in non-layered structures.

In layered structures, each layer typically has a thickness of 6~7 Å, which consists of a hexagonally packed layer of metal atoms sandwiched between two layers of chalcogen atoms. The intralayer M–X bonds are predominantly covalent in nature, whereas the sandwich layers are coupled by weak van der Waals forces thus allowing the crystal to readily cleave along the layer surface. Studies have shown that the single layers are stabilized by development of a ripple structure as in the case of graphene[23,24].

The metal atoms provide four electrons to fill the bonding states of TMDs such that the oxidation states of the metal (M) and chalcogen (X) atoms are +4 and −2, respectively. The lone-pair electrons of the chalcogen atoms terminate the surfaces of the layers, and the absence of dangling bonds renders those layers stable against reactions with environmental species. The M–M bond length varies between 3.15 Å and 4.03 Å, depending on the size of the metal and chalcogen ions. These values are 15–25% greater than the bond lengths found in elemental transition metal solids, indicating limited energetic and spatial overlap of the *d* orbitals in TMD compounds. The metal coordination of layered TMDs can be either trigonal prismatic or octahedral (typically distorted and sometimes referred to

---

[1]Materials Science and Engineering, Rutgers University, 607 Taylor Road, Piscataway, New Jersey 08854, USA. [2]Interdisciplinary School of Green Energy and Low Dimensional Carbon Materials Center, Ulsan National Institute of Science and Technology (UNIST), UNIST-gil 50, Ulsan 689-798, Republic of Korea. [3]Department of Physics, National University of Singapore, Singapore 117542. [4]Department of Chemistry, National University of Singapore, Singapore 117543. [5]Graphene Research Centre, National University of Singapore, Singapore 117546. [6]Institute of Atomic and Molecular Sciences, Academia Sinica, Taipei 10617, Taiwan. [7]School of Materials Science and Engineering, Nanyang Technological University, 50 Nanyang Avenue, Singapore 639798.
*e-mail: manish1@rci.rutgers.edu

© 2013 Macmillan Publishers Limited. All rights reserved

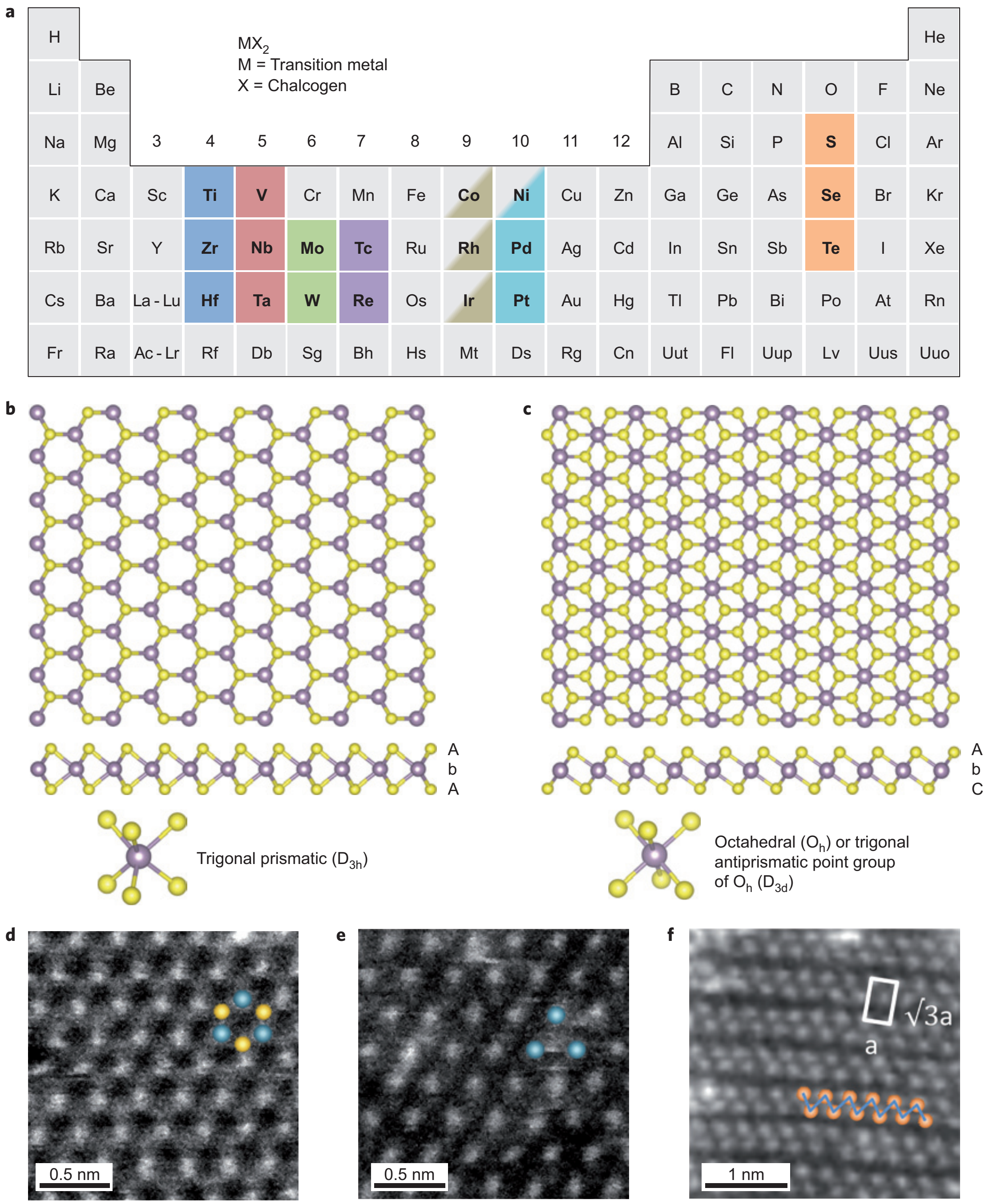

Figure 1 | Structure of monolayered TMDs. a, About 40 different layered TMD compounds exist. The transition metals and the three chalcogen elements that predominantly crystallize in those layered structure are highlighted in the periodic table. Partial highlights for Co, Rh, Ir and Ni indicate that only some of the dichalcogenides form layered structures. For example, NiS_2 is found to have apyrite structure but $NiTe_2$ is a layered compound. **b**,**c**, *c*-Axis and [11–20] section view of single-layer TMD with trigonal prismatic (**b**) and octahedral (**c**) coordinations. Atom colour code: purple, metal; yellow, chalcogen. The labels AbA and AbC represent the stacking sequence where the upper- and lower-case letters represent chalcogen and metal elements, respectively. **d**,**e**, Dark-field scanning transmission electron microscopy image of single-layer MoS_2 showing the contrast variation of 1H (**d**) and 1T (**e**) phases. Blue and yellow balls indicate Mo and S atoms, respectively. **f**, Zigzag chain clusterization of W atoms due to Jahn–Teller distortion in single layer WS_2. The clustered W atoms are represented by orange balls. The √3a x a unit cell of the superstructure is indicated with a white rectangle. Images in **d** and **e** reproduced with permission from ref. 12, © 2012 ACS. Image in **f** courtesy of T. Fujita.

as trigonal-antiprismatic) as shown in Fig. 1b and c, respectively. Depending on the combination of the metal and chalcogen elements, one of the two coordination modes is thermodynamically preferred.

In contrast to graphite, bulk TMDs exhibit a wide variety of polymorphs and stacking polytypes (a specific case of polymorphism) because an individual MX_2 monolayer, which itself contains three layers of atoms (X–M–X), can be in either one of the two phases. Most commonly encountered polymorphs are 1T, 2H and 3R where the letters stand for trigonal, hexagonal and rhombohedral, respectively, and the digit indicates the number of X–M–X units in the unit cell (that is, the number of layers in the stacking sequence). There are three different polytypes (that is, three different stacking sequences)

© 2013 Macmillan Publishers Limited. All rights reserved

for 2H polymorphs. A single TMD can be found in multiple polymorphs or polytypes, depending on the history of its formation. For example, natural MoS_2 is commonly found in the '2H phase' where the stacking sequence is AbA BaB (The capital and lower case letters denote chalcogen and metal atoms, respectively). Synthetic MoS_2, however, often contains the 3R phase where the stacking sequence is AbA CaC BcB (ref. 25). In both cases, the metal coordination is trigonal prismatic. Group 4 TMDs such as TiS_2 assume the 1T phase where the stacking sequence is AbC AbC and the coordination of the metal is octahedral. For the sake of simplicity, we will focus our attention on monolayer TMDs in the discussions below.

It should be highlighted that monolayer TMDs exhibit only two polymorphs: trigonal prismatic and octahedral phases. The former belongs to the D_{3h} point group whereas the latter belongs to the D_{3d} group. In the following discussion, they are referred to as monolayer 1H (or D_{3h})- and 1T (or D_{3d})- MX_2, respectively. These crystal phases can be differentiated using several techniques including high-resolution scanning transmission electron microscopy in annular dark field mode[12], as shown in Fig. 1d,e. Recent studies have shown that due to the lattice match of the 1H and 1T phases of MoS_2 and WS_2, coherent interfaces between domains of the two phases can also form[12]. Additional clustering can occur owing to distortions (for example the zig-zag chain-like patterns shown in Fig. 1f, and discussed at the end of this section).

The electronic structure of TMDs strongly depends on the coordination environment of the transition metal and its *d*-electron count; this gives rise to an array of electronic and magnetic properties as summarized in Table 1. In both 1H and 1T phases, the non-bonding *d* bands of the TMDs are located within the gap between the bonding (σ) and antibonding (σ^*) bands of M–X bonds as illustrated in Fig. 2a. Octahedrally coordinated transition metal centres (D_{3d}) of TMDs form degenerate d_{z^2,x^2-y^2} (e_g) and $d_{yz,xz,xy}$ (t_{2g}) orbitals that can together accommodate the TMDs' *d* electrons (a maximum of 6, for group 10 TMDs). On the other hand, the *d* orbitals of transition metals with trigonal prismatic coordination (D_{3h}) split into three groups, d_{z^2} (a_1), $d_{x^2-y^2,xy}$ (e), and $d_{xz,yz}$ (e′), with a sizeable gap (~1 eV) between the first two groups of orbitals. The diverse electronic properties of TMDs (see Table 1) arise from the progressive filling of the non-bonding *d* bands from group 4 to group 10 species. When the orbitals are partially filled, as in the case of 2H-$NbSe_2$ and 1T-ReS_2, TMDs exhibit metallic conductivity. When the orbitals are fully occupied, such as in 1T-HfS_2, 2H-MoS_2 and 1T-PtS_2, the materials are semiconductors. The effect of chalcogen atoms on the electronic structure is minor compared with that of the metal atoms, but a trend can still be observed: the broadening of the *d* bands and corresponding decrease in bandgap with increasing atomic number of the chalcogen. For example, the bandgap of 2H-MoS_2, 2H-$MoSe_2$ and 2H-$MoTe_2$ decreases gradually from 1.3 to 1.0 eV (ref. 25).

The preferred phase adopted by a TMD depends primarily on the *d*-electron count of the transition metal. Group 4 TMDs (featuring d^0 transition metal centres) are all in the octahedral structure whereas both octahedral and trigonal prismatic phases are seen in group 5 TMDs (d^1). Group 6 TMDs (d^2) are primarily found in trigonal prismatic geometry and group 7 TMDs (d^3) are typically in a distorted octahedral structure. Group 10 TMDs (d^6) are all in an octahedral structure.

It is well known that intercalation with alkali metals induces phase changes in some TMDs. For example, lithium intercalation in 2H-MoS_2 results in transformation to the 1T polymorph[25–28]. The reverse scenario of 1T to 2H transition has also been observed in TaS_2 on Li intercalation[29]. Destabilization of the original phase may be attributed to the effective change in the *d*-electron count — through transfer of an electron from the valence *s* orbital of the alkali metal to the *d* orbital of the transition metal centre — as well as the relative change in the free energy of the two phases. Recent studies have shown that the phase transformation can be partial, producing a 2H-1T hybrid structure[11,12]. Seifert and co-workers proposed that phase stabilization of 1T through substitutional doping may be a viable route to controlled local phase transformation, in turn achieving metal–semiconductor hybrid structures[30]. As 1T-MoS_2 and 1T-WS_2 exhibit metallic character, 1H-1T interfaces represent unique electronic heterojunctions across a chemically homogeneous layer, indicating a potential route to molecular electronics devices.

Table 1 | Electronic character of different layered TMDs[25].

Group	M	X	Properties
4	Ti, Hf, Zr	S, Se, Te	Semiconducting (E_g = 0.2~2 eV). Diamagnetic.
5	V, Nb, Ta	S, Se, Te	Narrow band metals ($\rho \sim 10^{-4}$ Ω.cm) or semimetals. Superconducting. Charge density wave (CDW). Paramagnetic, antiferromagnetic, or diamagnetic.
6	Mo, W	S, Se, Te	Sulfides and selenides are semiconducting (E_g ~1 eV). Tellurides are semimetallic ($\rho \sim 10^{-3}$ Ω cm). Diamagnetic.
7	Tc, Re	S, Se, Te	Small-gap semiconductors. Diamagnetic.
10	Pd, Pt	S, Se, Te	Sulfides and selenides are semiconducting (E_g = 0.4eV) and diamagnetic. Tellurides are metallic and paramagnetic. $PdTe_2$ is superconducting.

ρ, in-plane electrical resistivity.

In addition to phase transformation, several TMDs develop a periodic distortion of crystal lattice (reminiscent of a CDW) under certain conditions owing to instability in their electronic structure[22,31]. Typically, CDW phases are stable at low temperatures (<120 K for $TaSe_2$ and <40 K for $NbSe_2$) but this CDW-like lattice distortion has been observed at room temperature in some intercalated TMDs. The driving force for such distortions in TMDs is believed to be the 'Jahn–Teller instability' — in which the splitting of partially filled degenerate orbitals causes a reduction of the free energy[31]. The formation of a superlattice by chain clusterization of metal atoms has been observed at room temperature in Li-intercalated MoS_2 and WS_2; an example is shown in Fig. 1f[12]. Instead of the hexagonal arrangement with a 'a × a' unit cell (where a is the lattice parameter), a $\sqrt{3}$a × a (or 2a × a), $\sqrt{3}$a × $\sqrt{3}$a, or 2$\sqrt{3}$a × 2$\sqrt{3}$a superlattice is formed by shifting the atoms from their equilibrium position[32]. Interestingly, the distorted phase can be metastable even after the intercalant is removed[32]. The properties of such distorted TMDs are expected to be significantly different from that of their undistorted counterparts.

From three dimensions to two dimensions. Although a large body of work on bulk and chemically exfoliated TMDs has been conducted since the 1960s, a focused effort on deposition and isolation of high-quality single-layer nanosheets was re-initiated after the discovery of graphene[33]. Changes in interlayer coupling, degree of quantum confinement, and symmetry elements lead to dramatic differences in the electronic structure of single-layer TMDs compared with the bulk counterparts. The effect is particularly pronounced for semiconducting TMDs[4–14].

The band structures of materials can be calculated from first principles density functional theory (DFT) to gain further insight in their electronic structure. Figure 2b shows the band structures obtained for bulk and few- to mono-layer MoS_2, a group 6 TMD in trigonal prismatic structure. The bulk material is an indirect-gap semiconductor having a bandgap of ~1 eV with a valence band maximum (VBM) at the Γ point and a conduction band minimum (CBM) at the midpoint along Γ–K symmetry lines. In contrast, an

© 2013 Macmillan Publishers Limited. All rights reserved

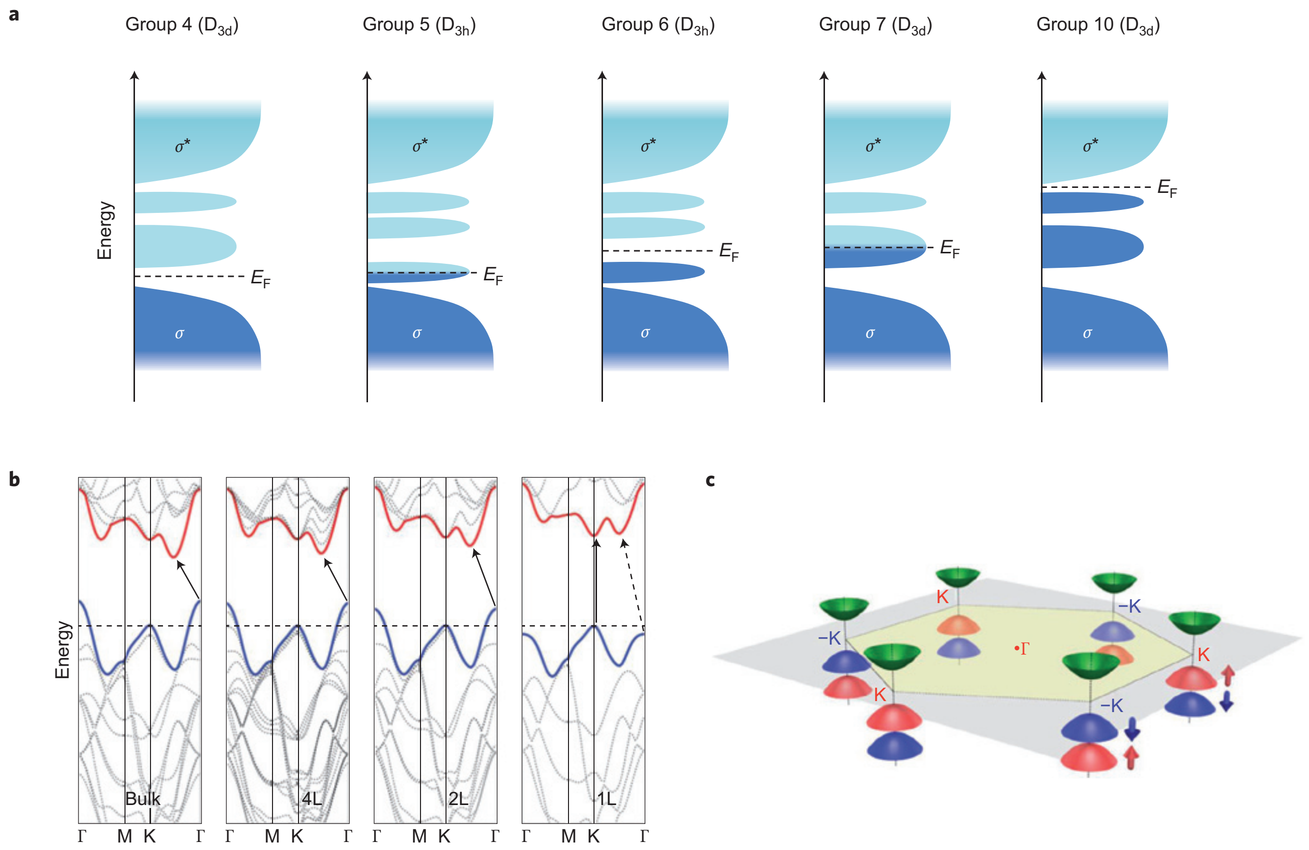

Figure 2 | *d*-Orbital filling and electronic character of various TMDs. a, Qualitative schematic illustration showing progressive filling of *d* orbitals that are located within the bandgap of bonding (σ) and anti-bonding states (σ^*) in group 4, 5, 6, 7 and 10 TMDs. D_{3h} and D_{3d} refer to the point group associated with the trigonal prismatic and the octahedral coordination of the transition metals (that is, the two monolayer polymorphs described in Fig. 1b). It should be noted that this simple model assumes ideal coordination; structural distortion often seen in many tellurides and group 7 TMDs lead to deviation in the electronic structure. The filled and unfilled states are shaded with dark and light blue, respectively. According to ligand field theory, D_{3d} compounds form two non-bonding *d* orbitals, $d_{yz,xz,xy}$ (bottom) and d_{z^2,x^2-y^2} (top), while D_{3h} (or O_h) compounds exhibit three *d* orbitals whose character is predomintly d_{z^2}, $d_{x^2-y^2,xy}$, and $d_{xz,yz}$ (from bottom to top). When an orbital is partially filled (such as in the case of group 5 and 7 TMDs), the Fermi level (E_F) is within the band and the compound exhibits a metallic character. When an orbital is fully filled (such as in group 6 TMDs), the Fermi level is in the energy gap and a semiconducting character is observed. **b**, Energy dispersion (energy versus wavevector *k*) in bulk, quadrilayer (4L), bilayer (2L) and monolayer (1L) MoS_2 from left to right. The horizontal dashed line represents the energy of a band maximum at the K point. The red and blue lines represent the conduction and valence band edges, respectively. The lowest energy transition (indicated by the solid arrows) is direct (vertical) only in the case of a single layer. Indirect transition in monolayer (dashed arrow in 1L plot) is greater in energy than the direct band edge transition (solid arrow). **c**, Band structure of MoS_2 showing six valleys and opposite spin–orbit splitting of the valence band at the K and K′ (-K) points. The red and blue surfaces represent spin-orbit-split valence band maxima, each of which is associated with a particular electron spin. The green surfaces represent the conduction band minima or the valleys. Figures reproduced with permission from: **b**, ref. 6, © 2010 ACS; **c**, ref. 36, © 2012 APS.

isolated monolayer of the same material is a direct-gap semiconductor with VBM and CBM coinciding at the K-point. This indirect-to-direct bandgap transition on going from a bulk to a monolayer material arises from quantum confinement effects. The transition is manifested as enhanced photoluminescence in monolayers of MoS_2, $MoSe_2$, WS_2 and WSe_2, whereas only weak emission is observed in multilayered form[5,6,11,34,35]. In the case of group 6 TMDs, the size of the monolayer bandgap is typically ~50% larger than that of bulk materials[6,36].

Recent theoretical calculations have revealed intriguing physics of spin and valley coupling in monolayer group 6 TMDs[36]. A valley quantum number is a property of an electron inside a crystal that is associated with the electron's momentum. Control of the valley degree of freedom allows manipulation of information, in a similar manner to spintronics and electronics, where the spin degree of freedom and the charge of an electron, respectively, are exploited. Broken inversion symmetry and spin–orbit coupling are properties of monolayer group 6 TMDs that allow access to the valley degree of freedom using circularly polarized light. There are two inequivalent momentum valleys (energy minima), *K* and *K*′ (or −*K*), among the six found at the corners of the first Brillouin zone of monolayer group 6 TMDs (Fig. 2c). The valence band at these valleys splits owing to strong spin–orbit coupling. For the monolayer MoS_2, time-reversal symmetry (a property in which motion is reversed when time is reversed) requires that the spin splitting at different valleys must be opposite, as shown in blue and red in Fig. 2c, where *K* and *K*′ show opposite situations. This leads to a unique situation where spin and valley degrees of freedom are coupled. When band edge electrons with a particular spin are excited with circularly polarized light, the electrons populate only one of the two valleys[7–9]. When these electrons relax to the ground state, they emit circularly polarized light, which is an indication that valley polarization is achieved and preserved during the process. The ability to achieve controlled valley polarization and its detection not only with light but also by other means (for example by electric field) could open up new ways for constructing switching 'valleytronic' devices.

© 2013 Macmillan Publishers Limited. All rights reserved

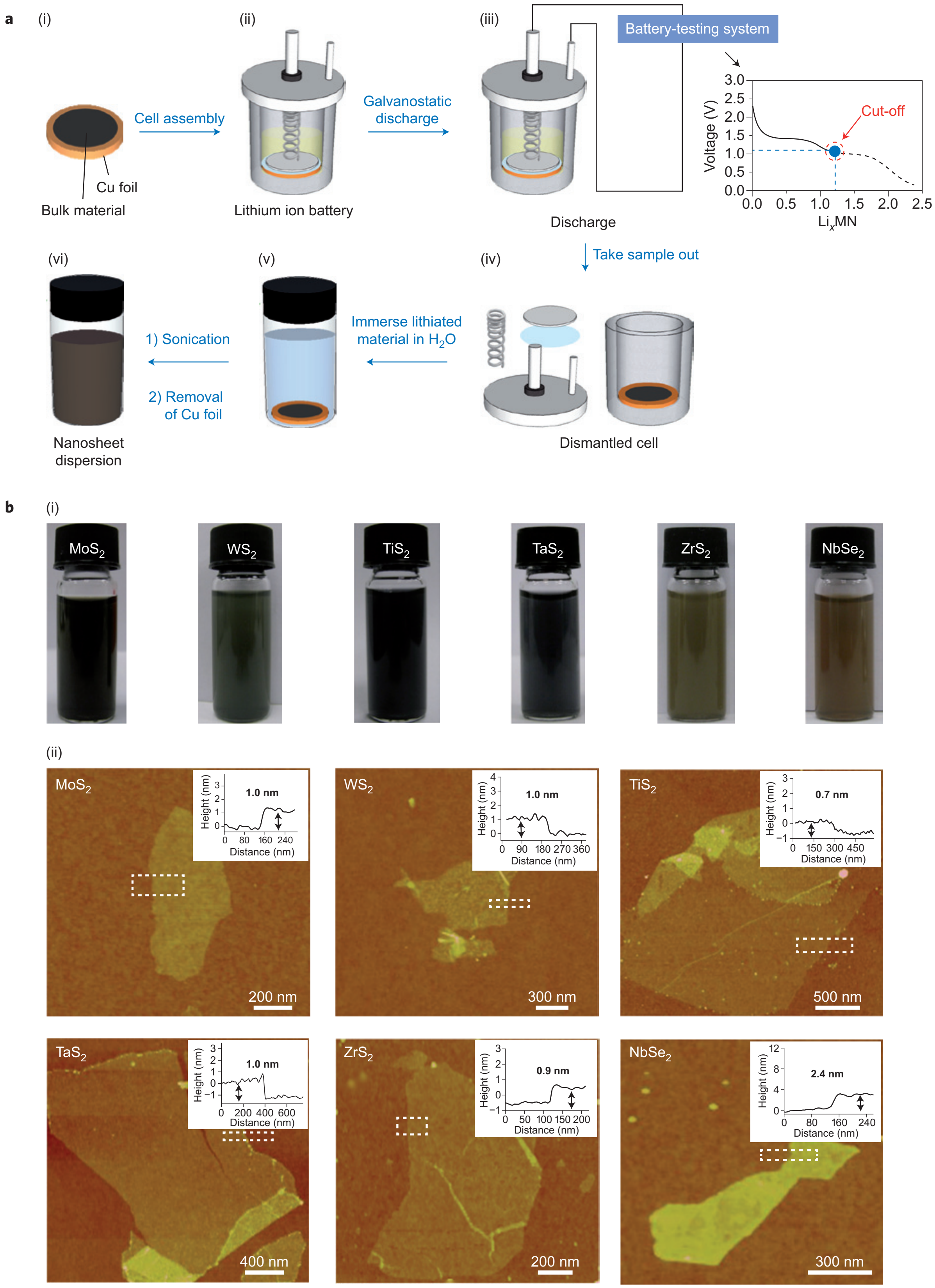

Figure 3 | Chemical exfoliation of monolayered TMDs. **a**, Schematic representation of the electrochemical lithiation process for synthesis of 2D nanosheets from layered bulk materials[47]. The cut-off voltage used to optimize the electrochemical lithiation conditions for preparation of few-layer BN, $NbSe_2$, WSe_2, Sb_2Se_3 and Bi_2Te_3 is also indicated. **b**, (i) Photographs of 2D nanosheet dispersions and (ii) the corresponding atomic force microscope images on SiO_2 substrates[42,47]. The insets of the AFM images represent height profiles from the substrate onto the nanosheets. The height of the step at the edge indicates the thickness of the nanosheets. Figures reproduced with permission from: **a**, **b**(i,ii) $NbSe_2$, ref. 47, © 2012 Wiley; **b**(i) MoS_2, WS_2, TiS_2, TaS_2, **b**(ii) WS_2, TiS_2, TaS_2, ZrS_2, ref. 42, © 2011 Wiley.

© 2013 Macmillan Publishers Limited. All rights reserved

Liquid exfoliation methods for preparation of 2D nanosheets

Mechanical exfoliation using the Scotch-tape method yields the highest-quality monolayered samples, which are ideal for demonstration of high-performance devices and condensed-matter phenomena[4,11,12,37–47]. Liquid exfoliation methods are likely to be better suited for fundamental and proof-of-concept demonstrations in applications where large quantities of materials are required, such as electrochemical energy storage, catalysis, sensing or fillers for composites. Liquid exfoliation by direct sonication in commonly used solvents such as dimethylformamide and *N*-methyl-2-pyrrolidone has been used to disperse graphene[48,49]. Recently, this method was employed to fabricate single-layer and multilayer nanosheets of a number of layered inorganic compounds, such as MoS_2, WS_2, $MoSe_2$, $NbSe_2$, $TaSe_2$, $NiTe_2$, $MoTe_2$, h-BN and Bi_2Te_3 (ref. 41).

To explore the relationship between the chemical structure of the exfoliated nanosheets and their stability in suspensions, the dispersion and exfoliation of four inorganic layered compounds (WS_2, MoS_2, $MoSe_2$ and $MoTe_2$) in a range of organic solvents were investigated[44]. Also, a number of layered crystals including BN, TMDs and transition metal oxides were successfully exfoliated in water. The nanosheets were dispersed by sonication in an aqueous solution of the surfactant sodium cholate, which coats the sheets, preventing their re-aggregation. These direct sonication techniques rely on the solvent or surfactant to overcome the cohesive energy between the neighbouring layers; which means the solvents must be chosen to have surface energies that are comparable to those of the material[45]. The key challenge of these methods is to enhance the yield of the single layers (as opposed to few-layers) and to maintain the lateral dimensions of the exfoliated sheets. Sonication has the detrimental effect of breaking the nanosheets (reducing their lateral dimensions) but the yield of moderately large (>1 μm) and thin nanosheets can be optimized with a careful choice of the starting mass, sonication time and centrifugation conditions[50]. Similar challenges have been overcome with graphene[48], which suggests that further progress in TMDs will also be possible.

One of the most effective methods for mass production of fully exfoliated TMD nanosheets is the ultrasound-promoted hydration of lithium-intercalated compounds. Recent reviews on this topic by Benavente and co-workers[39], and Golub and colleagues[40] provide additional details. Joensen and co-workers[37] demonstrated the preparation of single-layer MoS_2 with *n*-butyl lithium dissolved in hexane as the intercalation agent. An important step in the lithium intercalation process is the formation of Li_xXS_2 compound and this reaction can be tuned to control the yield of monolayers. The degree of lithiation also has implications on the amount of 1T phase present in MX_2. The lithiated solid product can then be retrieved by filtration and washed with hexane to remove excess lithium and organic residues from *n*-butyl lithium. The extracted product can be readily exfoliated by sonication in water. The yield of this method is very high (nearly 100% of the products are atomically thin) as suggested by our recent work on MoS_2 (ref. 11). The key advantage of the Li intercalation method is the ability to access the metallic 1T phase that is induced through charge transfer from Li to the TMD[11,12]. To accommodate this additional charge, a local rearrangement of the atomic structure from the 2H to the 1T phase occurs. The metastable 1T phase remains even in the solid form and the residual negative charge on the nanosheets is passivated by the presence of a water bilayer containing protons or residual Li ions. Our recent careful chemical analysis suggest that residual Li ions are not present so the excess charge stabilizing the 1T phase is likely to be due to the water bilayer. The current challenge is to control the location and amount of 1T phase through controlled exposure of single-layer TMD to Li.

Although the yield of the lithium intercalation method for obtaining single-layer TMDs is nearly 100%, some challenges remain. The first is that the experiment is carried out at high temperature (for example, 100 °C) for long durations (for example, three days). Also, the lithium intercalation must be carefully controlled to obtain complete exfoliation while preventing the formation of metal nanoparticles and precipitation of Li_2S. To address some of these challenges, the Zhang group[42] developed a simple method for the preparation of single-layer 2D nanosheets, such as MoS_2, WS_2, TiS_2 and TaS_2, through controllable lithium intercalation and subsequent exfoliation in water or ethanol, as shown in Fig. 3a. The advantage of this method is that lithium insertion can be monitored and precisely controlled so that the galvanostatic discharge can be stopped at the desired lithium content to avoid decomposition of the lithium-intercalated compounds. As a result, a series of high-quality 2D nanosheets have been successfully prepared. Following up this work, the same group[47] performed a systematic study of cut-off voltages required for the preparation of few-layer BN, $NbSe_2$, WSe_2, Sb_2Se_3 and Bi_2Te_3. Their results are summarized in Fig. 3b, which shows the stable 2D nanosheet dispersions and the AFM measurements of single-layer MoS_2, WS_2, TiS_2, TaS_2 and ZrS_2, and few-layer $NbSe_2$ nanosheets.

Chemical vapour deposition of single-layer TMDs

Chemical vapour deposition of graphene on copper has been a major breakthrough that has enabled the preparation of large-area graphene[51,52]. Very recently, synthesis of large-area ultrathin MoS_2 layers using CVD has been demonstrated using several approaches[4,53–57]. Most of the current CVD research has focused on MoS_2; we therefore introduce the details of MoS_2 growth by CVD, then discuss strategies for extending the methodology to other single-layered TMD materials.

A two-step thermolysis process shown in Fig. 4a was reported for deposition of three-layered MoS_2 sheets by dip-coating in ammonium thiomolybdates [$(NH_4)_2MoS_4$] and converting to MoS_2 by annealing at 500 °C followed by sulfurization at 1,000 °C in sulfur vapour[53]. The chemical reaction leading to the formation of the MoS_2 layers is $(NH_4)_2MoS_4 + H_2 \rightarrow 2NH_3 + 2H_2S + MoS_2$. The second annealing at 1,000 °C is required for improving the crystallinity (or the size of MoS_2 domains), so that the photoluminescence intensity and gate dependency in field-effect transistor (FET) devices can be observed. The FETs based on this material exhibited n-type behaviours with the ON/OFF current ratio ~10^5 and electron mobility up to 6 $cm^2\ V^{-1}s^{-1}$. This sample precursor was recently also used to grow epitaxial MoS_2 layers on graphene[55], as indicated in Fig. 4b.

A different strategy reported by Zhan and co-workers[56] for deposition of single-layer MoS_2 is based on the sulfurization of Mo metal thin films (Fig. 4c). Adsorption of sulfur on the Mo film to form MoS_2 has been studied since the 1970s[58,59], and it has been demonstrated through low-energy electron diffraction, auger electron spectroscopy and thermal desorption spectroscopy that sulfur atoms form ordered phases on the Mo crystal face[58]. Nuclei of MoS_2 appear in conjunction with chemisorbed sulfur species and then the film is formed by the diffusion of sulfur, which is affected by pressure and temperature[59].

Lee and co-workers have reported an alternative method for synthesizing large-area MoS_2 monolayer flakes using the gas-phase reaction of MoO_3 and S powders[57] (Fig. 4d). They conclude that treatment of substrates with aromatic molecules such as reduced graphene oxide, perylene-3,4,9,10-tetracarboxylic acid tetrapotassium salt (TPAS) and perylene-3,4,9,10-tetracarboxylic dianhydride (PTCDA) prior to deposition assists in the growth. The reaction mechanism in their study is likely to be: $MoO_3 + x/2S \rightarrow MoO_{3-x} + x/2SO_2$ and $MoO_{3-x} + (7-x)/2S \rightarrow MoS_2 + (3-x)/2SO_2$, where MoO_2 during the reaction is an intermediate phase formed when $x = 1$. However, full coverage of the substrate is a challenge using this method. Lin and co-workers have shown that wafer-scale deposition can be achieved using the same chemistry, where the few-layer MoS_2 was

© 2013 Macmillan Publishers Limited. All rights reserved

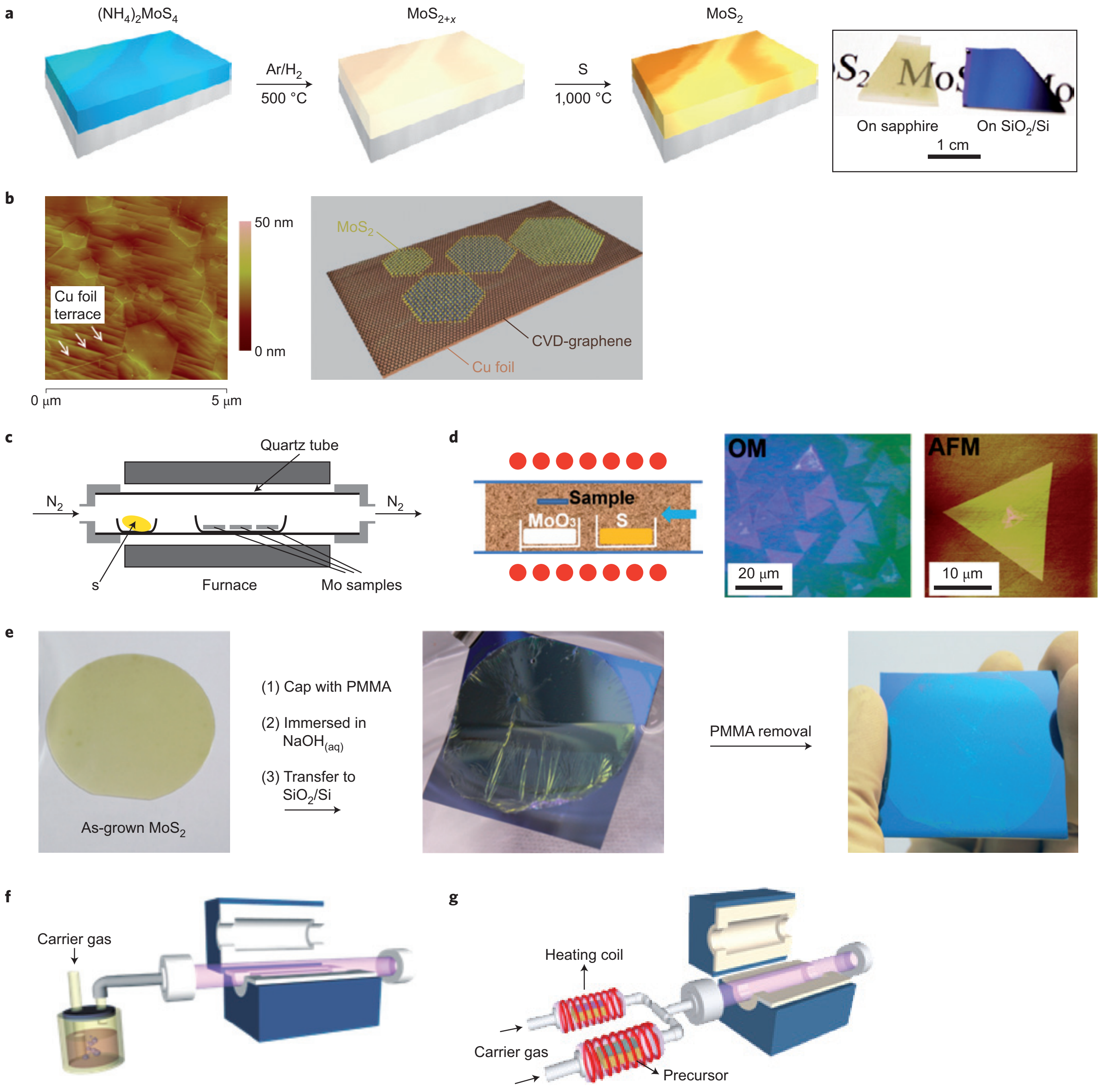

Figure 4 | Chemical vapour deposition of ultrathin TMDs. a, Schematic of MoS_2 layer deposited by two-step thermolysis, and the films obtained on a sapphire and silica sustrate[53]. **b**, MoS_2 nanosheets on CVD graphene/Cu substrates through van der Waals epitaxy[55]. **c**, Schematic illustration of single- to few-layered MoS_2 by sulfurization of Mo thin film[56]. **d**, Alternative method for the growth of a MoS_2 monolayer, also on a substrate (sample) from MoO_3 and S powders through a gas-phase reaction. The substrate has been treated with aromatic molecules to assist the growth of larger flakes, as shown by the optical micrograph and atomic force microscopic images of the triangular nanosheets that are obtained[57]. The red circles represent the heating reaction chamber. **e**, Wafer-scale deposition of mono- to few-layered MoS_2 films obtained by direct sulfurization of MoO_3 thin films, and their transfer onto arbitrary substrates[60]. **f**,**g**, CVD of ultrathin TMDs by vaporization and decomposition of a single precursor in solution (**f**) and by vaporization and decomposition of metal and chalcogen precursors in solid forms (**g**). Figures reproduced with permission from: **a**, ref. 53, © 2012 ACS; **b**, ref. 55, © 2012 ACS; **d**, ref. 57, © 2012 Wiley; **e**, ref. 60, © 2012 RSC.

obtained after direct sulfurization of MoO_3 thin-films on sapphire substrates (Fig. 4e)[60].

Despite initial reports showing promise, large-area and uniform growth of single-layer TMD by using CVD remains a challenge. Thus far selenization of Mo films for formation of $MoSe_2$ (ref. 61) and sulfurization of W (ref. 62) or WO_3 (ref. 63) film for WS_2 layers along with the aforementioned MoS_2 work have been demonstrated. However, substantial work on TMD thin films such as $MoSe_2$, WS_2, WSe_2, VSe_2 and TiS_2 has been performed in the past two decades and the conditions for growth of ultrathin TMD films are summarized in Table 2[64–68]. These previous techniques can be classified into three categories: (i) vaporization of metal and chalcogen precursors and their decomposition, followed by deposition of TMD on a substrate, (ii) direct sulfurization (or selenization) of metal film,

© 2013 Macmillan Publishers Limited. All rights reserved

NATURE CHEMISTRY DOI: 10.1038/NCHEM.1589

Table 2 | Summary of precursors and growth conditions of various TMDs obtained using chemical vapour deposition.

TMD	Precursor	Growth condition	Morphology
MoS_2 (ref. 53)	$(NH_4)_2MoS_4$[*] in DMF by bubbling with Ar	200 mTorr to 2 Torr at 400 °C	Hexagonal flake with 2 to 5 nm thickness
$MoSe_2$ (ref. 64)	$MoCl_5$ (heating at 255 °C) $C_8H_{18}Se$[†] (70 °C) or $C_4H_{10}Se$[‡] (90 °C)	Atmosphere at 450 ~ 600 °C	Thin film for $C_8H_{18}Se$ Needle-like structures for $C_4H_{10}Se$
WS_2 (ref. 65)	$WOCl_4$ (heating at 176 °C) $HS(CH_2)_2SH$[§] (heating at 63 °C)	Atmosphere at 250 ~ 600 °C	Thin film
WSe_2 (ref. 66)	$WOCl_6$ (heating at 260 °C) $C_4H_{10}Se$[‡] (heating at 70 °C)	Atmosphere at 450 ~ 600 °C	Plate-like crystallites mixed with needle-like crystal
VSe_2 (ref. 67)	$V(NMe_2)_4$[‖] (heating at 130 °C) $C_8H_{18}Se$[†] (heating at 90 °C)	Atmosphere at 250 ~ 500 °C	Thin hexagonal platelets
TiS_2 (ref. 68)	$Ti(NMe_2)_4$[¶] (heating at 150 °C) Bu^tSH[#] (57 °C) or $Bu_2{}^tS_2$[**] (115 °C)	Atmosphere at 300 ~ 600 °C	Thin film

[*] $(NH_4)_2MoS_4$: ammonium tetrathiomolybdate. [†] $C_8H_{18}Se$: di-*tert*-butylselenide. [‡] $C_4H_{10}Se$: diethylselenide. [§] $HS(CH_2)_2SH$: 1,2-ethanedithiol. [‖] $V(NMe_2)_4$: vanadium tetrakisdimethylamide. [¶] $Ti(NMe_2)_4$: tetrakis(dimethylamido)titanium. [#] Bu^tSH: 2-methylpropanethiol. [**] $Bu_2{}^tS_2$: *tert*-butyldisulfide

and (iii) conversion of MO_3 (metal oxide) to MS_2 (metal disulfide) by sulfurization. The typical CVD precursors are summarized in Table 2. These precursors can be fed into the reaction zone using the experimental schemes shown in Fig 4f,g.

Surface chemistry of single-layer TMDs

When MX_2 is exfoliated into thin sheets, the prismatic edges and basal planes are exposed, and edge termination by either M or X atoms is possible depending on the chemical potential of the growth environment. One important consequence of exfoliation is freeing the adjacent MX_2 layers from s–p_z orbital interaction, which causes the bandgap to widen. Changes in orbital hybridization also transform the single-layer MX_2 from indirect-bandgap to direct-bandgap semiconductors, thus giving rise to enhanced photoluminescence compared with the bulk material[5,6]. The exfoliated material exhibits chemistry that is defined by the type of coordination bond at the edges.

Another added dimension of controlling the surface chemistry of MX_2 is shape or size control. When the tri-layer X–M–X sheet is reduced in size laterally, it gives rise to nanosheets with low-coordination step-edges, kinks and corner atoms that induce additional local chemical effects. Once the atom density in the nanosheets drops below a critical threshold size, the effects of the edge and corner atoms can dominate over the basal plane atoms, so that the equilibrium shape of the cluster can be controlled by modifying the edge atoms[69]. The 'missing' coordination at the edges of MX_2 nanosheets (sometimes also referred to as 'open sites') gives rise to metallic edge states, which have important implications for catalysis, for example, as a substrate can coordinate to these edge metal centres. The quantum size effects also induce shifts in the valence band and the oxidation potentials, thus permitting catalytic activities not possible with the bulk band structure.

An example is triangular MoS_2 nanosheets synthesized by evaporating Mo atoms in the presence of H_2S gas, and affords a model system for understanding subtle effects like size-dependent catalytic properties. Lauritsen and Besenbacher applied scanning tunnelling microscopy (STM) to classify the size-dependent properties of such triangular MoS_2 nanocrystals grown on gold[70]. It turns out that the optimization of S excess or vacancies at the edges can critically influence the stability of the nanosheets. Sulfur vacancies were first generated with atomic hydrogen (illustrated in Fig. 5a) — they become the active sites in hydrodesulfurization. A particularly refractory sulfur-containing molecule that is one of the most challenging contaminants to remove from fuel, dibenzothiophene (DBT), was used as a probe molecule to test the catalytic activities of these MoS_2 nanosheets (as shown in Fig. 5b). Interestingly, detailed STM studies showed that the location of the S vacancies in the triangular clusters has direct consequences on their catalytic activity. For large-area nanosheets, energetics favour the formation of S vacancies on the edges, whereas for the small-sized sheets, they occur on the corners. The consequence, shown in Fig. 5c, is that steric constraints in the large nanosheets prevent DBT adsorption on the edge S vacancies, but unrestricted access to the corner S vacancy sites on small nanosheets allows favourable adsorption. In the case of small MoS_2 nanosheets, the shape of the material can be engineered by edge-plane functionalization because the equilibrium shape geometry is highly sensitive to the energetics of the edge atoms. This allows great tunability in the nanosheets' reactivity and electronic

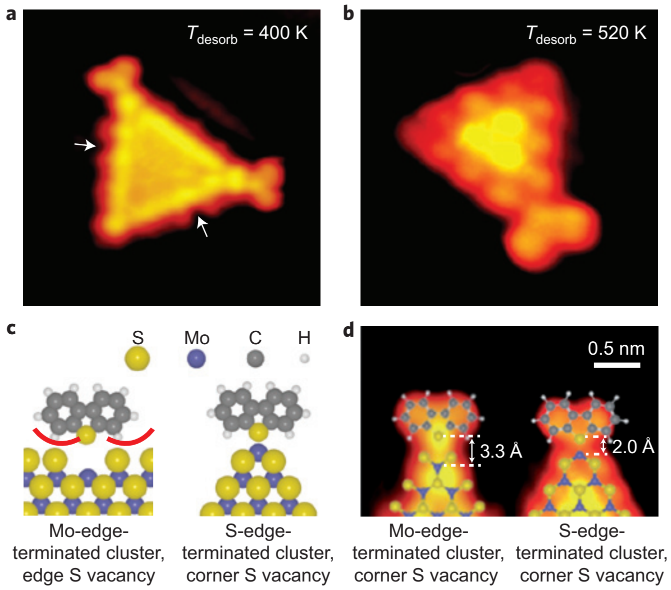

Figure 5 | Surface chemistry probed by adsorption of DBT. a, STM image (52 × 52 Å^2) of a Mo-edge-terminated cluster after dosing of DBT at 300 K. The white arrows indicate S vacancies. **b**, S-edge-terminated cluster after dosing of DBT at 300 K. The STM image is 22 × 22 Å^2. **c**, Illustrations of the adsorption of DBT on sites of Mo-edge-terminated (edge, left) and S-edge-terminated (corner, right) clusters with S vacancies[70]. The red curves in the case of the Mo-edge cluster show steric hindrance. **d**, STM images (15 × 15 Å^2) of the corner sites of a Mo- and S-edge S vacancy sites interacting with a DBT molecule. The distances between the S atom of DBT and the corner Mo atom show that the shape of the MoS_2material greatly influences its interaction with DBT, and the efficiency of its desulfurization. Figure reproduced with permission from ref. 70, © 2012 ACS.

© 2013 Macmillan Publishers Limited. All rights reserved

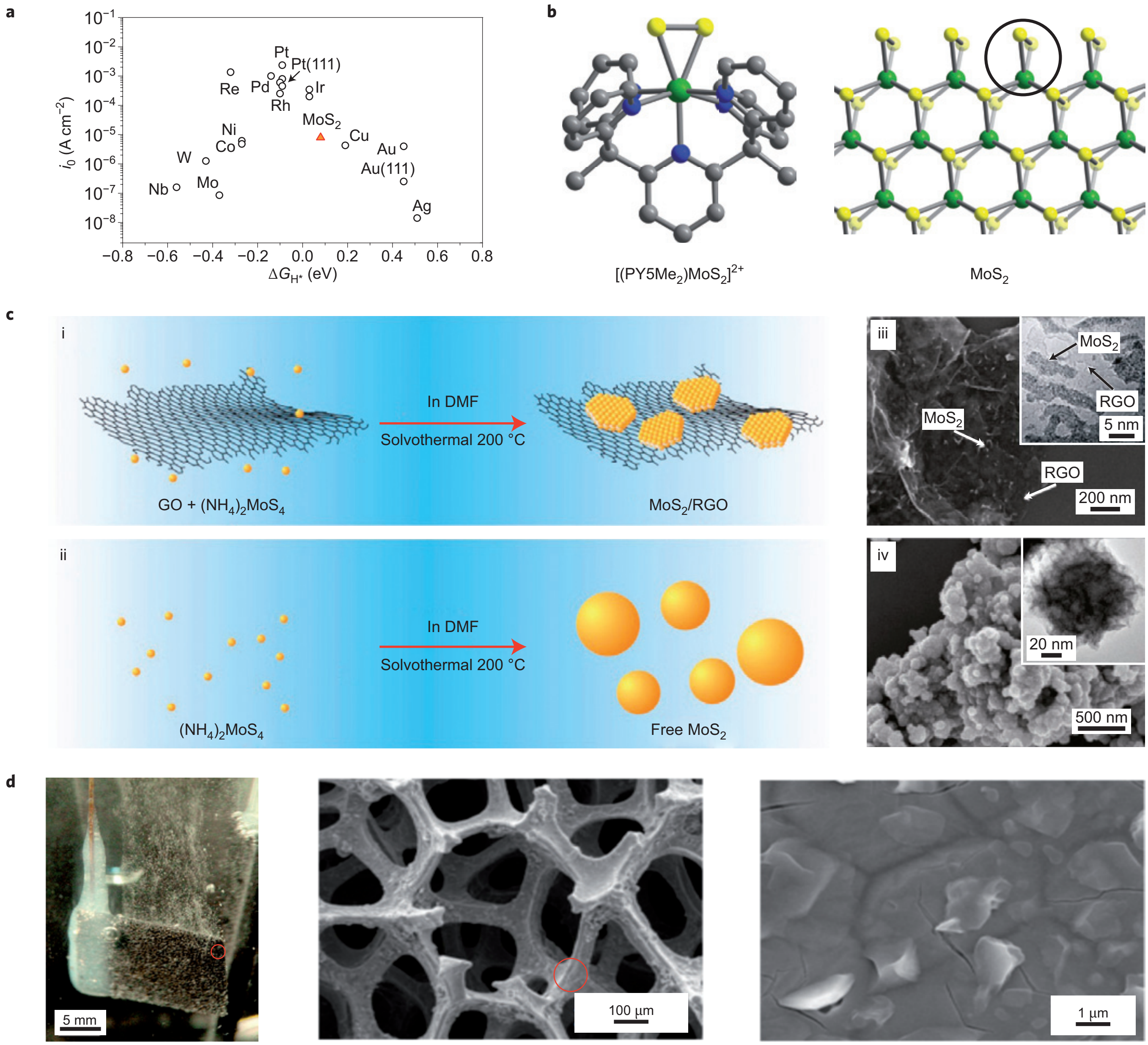

Figure 6 | Hydrogen evolution reaction catalysis with TMDs. a, Volcano plot of exchange current density (i_0)as a function of DFT-calculated Gibbs free energy (ΔG_{H^*}) of adsorbed atomic hydrogen for MoS_2 and pure metals[82]. **b**, [(PY$_5$Me$_2$)MoS$_2$]$^{2+}$ compound designed to mimic the edges of MoS_2. Colour code of the atoms: green, Mo; yellow, S; light blue, F; red, O; blue, N; and grey, C. H atoms are omitted for clarity[83]. **c**, (i,ii) Schematics of solvothermal synthesis (i) with graphene oxide sheets for MoS_2/RGO hybrid synthesis and (ii) without graphene oxide sheets, resulting in large, free MoS_2 particles. (iii,iv) SEM and TEM (inset) images of the MoS_2/RGO hybrid (iii) and of the free MoS_2 particles (iv)[75]. **d**, SEM images of graphene-protected Ni foam on which MoS_2 catalysts were grown[84]. Left, low magnification image of Ni foam coated with graphene and MoS_2. Middle, the region indicated by the red circle in the left image has been magnified to show the skeleton structure of the foam. Right, magnified region from the red circle in the central image, showing the graphene/MoS_2 films on the polycrystalline Ni foam. Figures reproduced with permission from: **a**, ref. 82, © 2007 AAAS; **b**, ref. 83, © 2012 AAAS; **c**, ref. 75, 2011 ACS; **d**, ref. 84, © 2012 Wiley.

properties (Fig. 5d). An important implication for the high density of reactive edges is the possibility of modifying the catalytic reactivity of the MoS_2 by edge-site substitution with transition metals like Co or Ni to form bimetallic catalytic sites.

Previous STM studies on MoS_2 monolayered nanosheets have shown that edge modification is responsible for the enhanced catalytic activity in hydrodesulfurization catalysis[71]. When promoter atoms like Ni and Co adsorb on the edge of MoS_2, they modify the edge-plane coordination and change the equilibrium shape of MoS_2 nanoclusters, which in turn alters the affinity of molecules to bind to these sites through thiol groups[72].

Hydrogen evolution reaction

The identification of the low-cost TMD materials as potential electrocatalysts for the hydrogen evolution reaction (HER; $2H^+ + e^- \rightarrow H_2$) has opened up exciting paths in this area[73,74]. However, their bulk form has not been very efficient in HER, and nanostructuring TMDs has been used to enhance the concentration of catalytically active edges. Density functional theory calculations have also indicated that the edges of MoS_2 nanosheets are active for HER[75–77]. The HER activity of various catalysts can be summarized in the 'volcano plot', where the exchange current density for different catalytic metals in acids is plotted as a function of the DFT-calculated metal–hydrogen

© 2013 Macmillan Publishers Limited. All rights reserved

bond strength (or Gibbs free energy of absorbed atomic hydrogen on metals; Fig. 6a). The HER activity reaches a peak value at intermediate bond strengths for several rare metals including Pt, Rh, Re and Ir. To find suitable replacement catalysts that are inexpensive, electrochemically stable and environmentally friendly for the currently used costly Pt, Norskøv and co-workers used DFT to build a predictive model of HER activity based on the calculated adsorption energies[78,79]. According to their calculations, a reasonably high activity for edge sites on lamellar MoS_2 was predicted[80,81]. The result showed that the hydrogen binding energy of MoS_2 is located close to the top of the volcano curve, which was subsequently verified by electrochemical measurements as shown in Fig. 6a[82]. Much of the experimental work has stemmed from theoretical considerations that suggested the metallic edges of trigonal prismatic (2H) MoS_2 crystals are electrocatalytically active whereas the basal plane remains inert. Jaramillo and co-workers have proved experimentally that the dominant edge structure in 2H MoS_2 nanostructures is the sulfide-terminated Mo-edge (referred to as the sulfided Mo-edge), and that it is the active site for HER[82]. Recently, Karunadasa reported the synthesis of a well-defined Mo^{IV}-disulfide inorganic compound $[(PY_5Me_2)MoS_2]^{2+}$ as shown in Fig. 6b, which mimics the disulfide-terminated edge sites of MoS_2 in catalytic hydrogen generation[83]. The strength of this approach is that bimetallic organometallic complexes with terminal sulfur ligands may be synthesized in future from Mo, Co, W complexes, thus affording a rational approach for making powerful molecular catalysts.

The Tafel slope, determined by electrode potential versus the logarithm of the current density, and usually reported in mV per decade, is typically used as a measure of the potential increase required to increase the resulting current at the cathode by one order of magnitude. Several recent reports have shown that the Tafel slopes for the HER are similar when using monolayer MoS_2 flakes and nanoparticles, ranging from 40 to 60 mV per decade[75]. Li and co-workers employed a template-assisted method to synthesize MoS_2 nanoclusters with a high density of reactive edges, on reduced graphene oxide (RGO)[75]. In this case, RGO acts as a template for the nucleation and growth of planar MoS_2 nanosheets, which would otherwise aggregate into spherical forms in solution (see Fig. 6c). The more conducting RGO substrate also improves the charge-transfer kinetics from the MoS_2 nanosheet catalysts to the electrode, resulting in a Tafel slope of 41 mV per decade.

Thus far, the edge of the TMD materials has been recognized as the active site for HER. However, if it is the metallic nature of the sulfide edge that is responsible for the enhanced catalytic activity, then the presence of the metallic 1T phase in the Li-exfoliated MX_2 TMDs should substantially enhance the catalytic activity. However, the catalytic property for the 1T phase remains an important and open question that requires more investigation. Calculations on MoS_2 have shown that only a quarter of the edge sites are active for hydrogen production. Increasing the number of active edge sites per unit area or volume by modifying the atomic structure or the nanostructure, or by changing the electronic structure of the system to increase the enthalpy of hydrogen adsorption, or even by incorporating the TMD nanosheets into conducting nano- or micro-sized templates, have remained important issues for efficient hydrogen production. A recent study has demonstrated efficient electrocatalytic hydrogen generation using MoS_x catalysts supported by a three-dimensional Ni foam, deposited with graphene layers as a microporous supporting template (such as the one shown in Fig. 6d). Here, the graphene layer was used as an interface to provide robust protection of Ni against corrosion from acid[84]. This approach could lead to tailored geometrically designed electrodes that not only increase the activity of the catalysts but also facilitate the reaction kinetics.

The stability of MX_2 against photocorrosion is advantageous in photochemical reactions compared with materials such as CdS. The variable bandgap of different MX_2 materials suggests that they can harvest light over a wide range from ultraviolet to infrared wavelengths. Their optical properties can be also be tuned by size confinement and functionalization[85]. All these attributes suggest that MX_2 are attractive in photochemical water-splitting and battery applications, where the metallic edge effects are useful in charge transfer and the basal plane inactivity protects against electrolyte decomposition. Increasing evidence suggests that when MoS_2 is hybridized with other materials, superior performance in electrocatalytic- or charge-storage applications can be obtained due to synergistic interactions. In the absence of a noble-metal co-catalyst, Xiang and co-workers demonstrated the cooperative effect of the $TiO_2/MoS_2/$graphene composite for water splitting, achieving a high H_2 production rate of 165.3 μmol h^{-1} when the content of the MoS_2/graphene co-catalyst is 0.5 wt%. Increasing the content of graphene in this co-catalyst to 5.0 wt% increases the apparent quantum efficiency to 9.7% at 365 nm (ref. 86). Furthermore, by using a hydrothermal method, Zhang and colleagues synthesized few-layer MoS_2 nanosheets coated on TiO_2 nanobelts, which showed high photocatalytic hydrogen production even without the Pt co-catalyst[87].

Energy storage applications

The interlayer spacing of TMDs provides a convenient environment for the accommodation of a variety of guest species, for example Li^+ ions. Bulk TMD materials such as MoS_2 and WS_2 have been investigated as electrode materials for lithium ion batteries because Li^+ ions can be easily intercalated or extracted from these materials[88,89]. But lithiation of these compounds leads to structural instability during the exfoliation step, as described above. Furthermore, their relatively low average voltage and energy density limits their potential as cathode materials[88]. In contrast, exfoliated nanosheets are in some ways very attractive as anodes for lithium ion batteries, and do not suffer from the structural instability of bulk crystals because the nanosheets are loosely stacked and can accommodate structural changes.

The electrical conductivity of TMDs (both in bulk and exfoliated forms), however, is too low for their effective implementation as electrodes. Besides conductivity, other factors such as morphology, structure and particle size have been shown to be important parameters in the performance of TMDs as anodes in lithium ion batteries. For MoS_2/graphene composites, a Mo:C molar ratio of 1:2 exhibits the highest specific capacity of ~1,100 mAh g^{-1} at a current of 100 mA g^{-1}, as well as good cycling stability and high-rate capability. The superior electrochemical performance of MoS_2/graphene composites as lithium ion battery anodes is attributed to their robust composite structure and the synergistic effects between layered MoS_2 and graphene[90–93]. It is interesting to note that the coulombic efficiency of MoS_2 as an anodic material is much higher than those of graphene oxide and its derivatives in lithium ion batteries. This may be due to the basal plane inactivity of MoS_2 that discourages surface trapping of lithium compared with graphene oxide-based materials that have highly reactive oxygen functionalities.

The cycling stability of the TMD electrodes remains challenging, but can be enhanced by integration with carbonaceous materials through deposition of MoS_2 layers on thermally carbonized organic conducting polymers[94] and carbon nanotubes[95], or by coating carbon onto TMDs using CVD[96]. The deposition of carbon onto TMDs extends cycling stability through an enhancement of the electrical conductivity. A similar effect can also be achieved by forming electrodes that consist of graphene/MoS_2 hybrid nanosheets[97,98]. Loss that occurs during the first cycle is still the major issue for TMD-based anodes, and must be minimized if TMD nanosheets are to become useful for energy storage applications.

Single-layer TMDs for high-performance electronics

There has also been substantial interest in utilizing 2D TMD nanosheets for FETs and other high-performance devices. Electronic properties and device integration are discussed in a

© 2013 Macmillan Publishers Limited. All rights reserved

recent review[4] and other contributions[99–107], so we only mention a few key points here. The results from MoS_2 monolayer FET devices show excellent ON/OFF current ratio (>10^7), the absence of short channel effects and exceptionally low sub-threshold swing (~60–70 mV per decade)[100]. These characteristics make them ideal for back-plane-switching FETs in the next generation of low-power and transparent displays.

In addition to high-performance logic devices, monolayered TMD nanosheets are also ideal for large-area electronics that are flexible and transparent. The bendability of the CVD-grown MoS_2 layers has been demonstrated on highly flexible thin-film transistors. Pu and co-workers fabricated a MoS_2 FET with ion gel dielectrics on a flexible polyimide substrate[108]. The FET device exhibited good electrical performance with an ON/OFF ratio of 10^5, mobility of 12.5 $cm^2\ V^{-1}\ s^{-1}$, a low operating voltage of 0.68 V and a remarkably high mechanical flexibility. In addition to flexible electronics, coupling the fast optical response with high mobility should also lead to sensitive photodetectors[109].

Conclusions and outlook

The rich chemistry of mono- and few-layered TMDs offers many opportunities for the investigation of fundamental phenomena and their practical purposes. The diversity of the materials that are accessible and their versatile and tunable properties make them attractive for a wide range of applications from energy storage and catalysis for hydrogen evolution to opto-electronics. In this Review, we have highlighted some key features of TMDs when they are exfoliated into single or a few layers. Scalable exfoliation using chemicals will enable the large-scale synthesis of sheets with controlled structures and functionalities, although CVD methods are still to be developed for growing single and uniform monolayered sheets over large areas. It is also important to devise routes to control the doping of TMDs to construct p- and n-type heterostructures for electronics, spintronics and valleytronics. The surface chemistry of single-layer TMDs has proved crucial in processes such as photochemical water-splitting, electrocatalytic hydrogen evolution and energy storage. Several other key challenges remain that must be resolved in the near term: electrical conductance and cycling stability of TMD nanosheets must be enhanced for use as electrodes for energy storage. The density of active sites must also be improved for catalysis — this would make the entire basal plane of the TMD nanosheets catalytically active, rather than just the edges. Finally, controlled and well designed heterostructures must be synthesized for implementation into electronic devices. The vast number of possibilities in terms of designing and fabricating different compounds, and integrating them in hetero-lattices vertically and laterally to achieve tailored properties for specific applications, will require substantial interactions between experimentalists and theorists.

References

1. Novoselov, K. S. *et al.* Electric field effect in atomically thin carbon film. *Science* **306,** 666–669 (2004).
2. Castro Neto, A. H., Guinea, F., Peres, N. M. R., Novoselov, K. S. & Geim, A. K. The electronic properties of graphene. *Rev. Mod. Phys.* **81,** 109–162 (2009).
3. Geim, A. K. Graphene: Status and prospects. *Science* **324,** 1530–1534 (2009).
4. Wang, Q. H., Kalantar-Zadeh, K., Kis, A., Coleman, J. N. & Strano, M. S. Electronics and opto-electronics of two-dimensional transition metal dichalcogenides. *Nature Nanotech.* **7,** 699–712 (2012).
5. Mak, K. F., Lee, C., Hone, J., Shan, J. & Heinz, T. F. Atomically thin MoS_2: A new direct-gap semiconductor. *Phys. Rev. Lett.* **105,** 136805 (2010).
6. Splendiani, A. *et al.* Emerging photoluminescence in monolayer MoS_2. *Nano Lett.* **10,** 1271–1275 (2010).
7. Cao, T. *et al.* Valley-selective circular dichroism of monolayer molybdenum disulphide. *Nature Commun.* **3,** 887 (2012).
8. Zeng, H., Dai, J., Yao, W., Xiao, D. & Cui, X. Valley polarization in MoS_2 monolayers by optical pumping. *Nature Nanotech.* **7,** 490–493 (2012).
9. Mak, K. F., He, K., Shan, J. & Heinz, T. F. Control of valley polarization in monolayer MoS_2 by optical helicity. *Nature Nanotech.* **7,** 494–498 (2012).
10. Li, H. *et al.* Optical identification of single- and few-layer MoS_2 sheets. *Small* **8,** 682–686 (2012).
11. Eda, G. *et al.* Photoluminescence from chemically exfoliated MoS_2. *Nano Lett.* **11,** 5111–5116 (2011).
12. Eda, G., Fujita, T., Yamaguchi, H., Voiry, D., Chen, M. W. & Chhowalla, M. Coherent atomic and electronic heterostructures of single-layer MoS_2. *ACS Nano* **6,** 7311–7317 (2012).
13. Yin, Z. *et al.* Single-layer MoS_2 phototransistors. *ACS Nano* **6,** 74–80 (2012).
14. Castellanos-Gomez, A. *et al.* Laser-thinning of MoS_2: On demand generation of a single-layer semiconductor. *Nano Lett.* **12,** 3187–3192 (2012).
15. Feng, J. *et al.* Giant moisture responsiveness of VS_2 ultrathin nanosheets for novel touchless positioning interface. *Adv. Mater.* **24,** 1969–1974 (2012).
16. Matte, H. S. S. *et al.* MoS_2 and WS_2 analogues of graphene. *Angew. Chem. Int. Ed.* **49,** 4059–4062 (2010).
17. Li, H. *et al.* Fabrication of single- and multilayer MoS_2 film-based field effect transistors for sensing NO at room temperature. *Small* **8,** 63–67 (2012).
18. Loh, K. P., Bao, Q. L., Eda, G. & Chhowalla, M. Graphene oxide as a chemically tuneable platform for optical applications. *Nature Chem.* **2,** 1015–1024 (2010).
19. Sipos, B. *et al.* From Mott state to superconductivity in 1T-TaS_2. *Nature Mater.* **7,** 960–965 (2008).
20. Gordon, R. A., Yang, D., Crozier, E. D., Jiang, D. T. & Frindt, R. F. Structures of exfoliated single layers of WS_2, MoS_2, and $MoSe_2$ in aqueous suspension. *Phys. Rev. B* **65,** 125407 (2002).
21. Kuc, A., Zibouche, N. & Heine, T. Influence of quantum confinement on the electronic structure of the transition metal sulfide TS_2. *Phys. Rev. B* **83,** 245213 (2011).
22. Wilson, J. A., Di Salvo, F. J. & Mahajan, S. Charge-density waves and superlattices in the metallic layered transition metal dichalcogenides. *Adv. Phys.* **24,** 117–201 (1975).
23. Meyer, J. C., Geim, A. G., Katnelson, M. I., Novoselov, K. S. & Roth, S. The structure of suspended graphene sheets. *Nature* **446,** 60–63 (2006).
24. Bertolazzi, S., Brivio, J. & Kis, A. Stretching and breaking of ultrathin MoS_2. *ACS Nano* **5,** 9703–9709 (2011).
25. Wilson, J. A. & Yoffe, A. D. The transition metal dichalcogenides discussion and interpretation of optical, electrical and structural properties. *Adv. Phys.* **18,** 193–335 (1969).
26. Bissessur, R., Kanatzidis, M. G., Schindler, J. L. & Kannewurf, C. R. Encapsulation of polymers into MoS_2 and metal to insulator transition in metastable MoS_2. *J. Chem. Soc. Chem. Commun.* 1582–1585 (1993).
27. Frindt, R. F. & Yoffe, A. D. Physical properties of layer structures: Optical properties and photoconductivity of thin crystals of molybdenum disulphide. *Proc. R. Soc. Lond. A* **273,** 69–83 (1963).
28. Py, M. A. & Haering, R. R., Structural destabilization induced by lithium intercalation in MoS_2 and related-compounds. *Can. J. Phys.* **61,** 76–84 (1983).
29. Ganal, P., Olberding, W. & Butz, T. Soft chemistry induced host metal coordination change from octahedral to trigonal prismatic 1T-TaS_2. *Solid State Ionics* **59,** 313–319 (1993).
30. Lorenz, T., Teich, D., Joswig, J. O. & Seifert, G. Theoretical study of mechanical behavior of individual TiS_2 and MoS_2 nanotubes. *J. Phys. Chem. C* **116,** 11714–11721 (2012).
31. Castro Neto, A. H. Charge density wave, superconductivity, and anomalous metallic behavior in 2D transition metal dichalcogenides. *Phys. Rev. Lett.* **86,** 4382–4385 (2001).
32. Heising, J. & Kanatzidis, M. G. Exfoliated and restacked MoS_2 and WS_2: Ionic or neutral species? Encapsulation and ordering of hard electropositive cations. *J. Am. Chem. Soc.* **121,** 11720–11732 (1999).
33. Castro Neto, A. H. & Novoselov, K. Two dimensional crystals: Beyond graphene. *Mater. Exp.* **1,** 10–17 (2011).
34. Tongay, S. *et al.* Thermally driven crossover from indirect toward direct bandgap in 2D semiconductors: $MoSe_2$ versus MoS_2. *Nano Lett.* **12,** 5576–5580 (2012).
35. Zhao, W. *et al.* Evolution of electronic structure in atomically thin sheets of WS_2 and WSe_2. *ACS Nano* **7,** 791–797 (2013).
36. Xiao, D., Liu, G.-B., Feng, W., Xu, X. & Yao, W. Coupled spin and valley physics in monolayers of MoS_2 and other group-VI dichalcogenides. *Phys. Rev. Lett.* **108,** 196802 (2012).
37. Joensen, P., Frindt, R. F. & Morrison, S. R. Single-layer MoS_2. *Mater. Res. Bull.* **21,** 457–461 (1986).
38. Dines, M. B. Lithium intercalation via n-butyllithium of layered transition-metal dichalcogenides. *Mater. Res. Bull.* **10,** 287–291 (1975).
39. Benavente, E., Santa Ana, M. A., Mendizabal, F. & Gonzalez, G. Intercalation chemistry of molybdenum disulfide. *Coord. Chem. Rev.* **224,** 87–109 (2002).

© 2013 Macmillan Publishers Limited. All rights reserved

40. Golub, A. S., Zubavichus, Y. V., Slovokhotov, Y. L. & Novikov, Y. N. Single-layer dispersions of transition metal dichalcogenides in the synthesis of intercalation compounds. *Russian Chem. Rev.* **72,** 123–141 (2003).
41. Coleman, J. N. *et al.* Two-dimensional nanosheets produced by liquid exfoliation of layered materials. *Science* **331,** 568–571 (2011).
42. Zeng, Z. Y. *et al.* Single-layer semiconducting nanosheets: High-yield preparation and device fabrication. *Angew. Chem. Int. Ed.* **50,** 11093–11097 (2011).
43. Zhou, K.-G., Mao, N.-N., Wang, H.-X., Peng, Y. & Zhang, H.-L. A mixed-solvent strategy for efficient exfoliation of inorganic graphene analogues. *Angew. Chem. Int. Ed.* **50,** 10839–10842 (2011).
44. Cunningham, G. *et al.* Solvent exfoliation of transition metal dichalcogenides: Dispersibility of exfoliated nanosheets varies only weakly between compounds. *ACS Nano* **6,** 3468–3480 (2012).
45. Smith, R. J. *et al.* Large-scale exfoliation of inorganic layered compounds in aqueous surfactant solutions. *Adv. Mater.* **23,** 3944–3948 (2011).
46. May, P., Khan, U., Hughes, J. M. & Coleman, J. N. Role of solubility parameters in understanding the steric stabilization of exfoliated two-dimensional nanosheets by adsorbed polymers. *J. Phys. Chem. C* **116,** 11393–11400 (2012).
47. Zeng, Z. *et al.* An effective method for the fabrication of few-layer-thick inorganic nanosheets. *Angew. Chem. Int. Ed.* **51,** 9052–9056 (2012).
48. Hernandez, Y. *et al.* High-yield production of graphene by liquid-phase exfoliation of graphite. *Nature Nanotech.* **3,** 563–568 (2008).
49. Zhi, C., Bando, Y., Tang, C., Kuwahara, H. & Goldberg, D. Large scale fabrication of boron nitrode nanosheets and their utilization in polymeric composites with improved thermal and mechanical properties. *Adv. Mater.* **21,** 2889–2893 (2009).
50. O'Neill, A., Khan, U. & Coleman, J. N. Preparation of high concentration dispersions of exfoliated MoS_2 with increased flake size. *Chem. Mater.* **24,** 2414–2421 (2012).
51. Li, X. *et al.* Large-area synthesis of high-quality and uniform graphene films on copper foils. *Science* **324,** 1312–1314 (2009).
52. Bae, S. *et al.* Roll-to-roll production of 30-inch graphene films for transparent electrodes. *Nature Nanotech.* **5,** 574–578 (2010).
53. Liu, K.-K. *et al.* Growth of large-area and highly crystalline MoS_2 thin layers on insulating substrates. *Nano Lett.* **12,** 1538–1544 (2012).
54. Lee, H. S. *et al.* MoS_2 Nanosheet phototransistors with thickness-modulated optical energy gap. *Nano Lett.* **12,** 3695–3700 (2012).
55. Shi, Y. *et al.* Van der waals epitaxy of MoS_2 layers using graphene as growth templates. *Nano Lett.* **12,** 2784–2791 (2012).
56. Zhan, Y., Liu, Z., Najmaei, S., Ajayan, P. M. & Lou, J. Large-area vapor-phase growth and characterization of MoS_2 atomic layers on a SiO_2 substrate. *Small* **8,** 966–971 (2012).
57. Lee, Y.-H. *et al.* Synthesis of large-area MoS_2 atomic layers with chemical vapor deposition. *Adv. Mater.* **24,** 2320–2325 (2012).
58. Salmeron, M., Somorjai, G. A. & Chianelli R. R. A LEED-AES study of the structure of sulfur monolayers on the Mo(100) crystal face. *Surf. Sci.* **127,** 526–540 (1983).
59. Wilson, J. M. LEED and AES study of the interaction of H_2S and Mo (100). *Surf. Sci.* **53,** 330–340 (1975).
60. Lin, Y.-C. *et al.* Wafer-scale MoS_2 thin layers prepared by MoO_3 sulfurization. *Nanoscale* **4,** 6637–6641 (2012).
61. Jager-waldau, A., Lux-steiner, M., Jager-waldau, R., Burkhardt, R. & Bucher, E. Composition and morphology of $MoSe_2$ thin films. *Thin Solid Films* **189,** 339–345 (1990).
62. Genut, M., Margulis, L., Tenne, R. & Hodes, G. Effect of substrate on growth of WS_2 thin films. *Thin Solid Films* **219,** 30–36 (1992).
63. Ennaoui, A., Fiechter, S., Ellmer, K., Scheer, R. & Diesner, K. Preparation of textured and photoactive 2H-WS_2 thin films by sulfurization of WO_3. *Thin Solid Films* **261,** 124–131 (1995).
64. Boscher, N. D., Carmalt, C. J., Palgrave, R. G., Gil-Tomas, J. J. & Parkin. I. P. Atmospheric pressure CVD of molybdenum diselenide films on glass. *Chem. Vapor. Depos.* **12,** 692–698 (2006).
65. Carmalt, C. J., Parkin, I. P. & Peters. E. S. Atmospheric pressure chemical vapour deposition of WS_2 thin films on glass. *Polyhedron* **22,** 1499–4505 (2003).
66. Boscher, N. D., Carmalt, C. J. & Parkin. I. P. Atmospheric pressure chemical vapor deposition of WSe_2 thin films on glass–highly hydrophobic sticky surfaces. *J. Mater. Chem.* **16,** 122–127 (2006).
67. Boscher, N. D., Blackman, C. S., Carmalt, C. J., Parkin, I. P. & Prieto. A. G. Atmospheric pressure chemical vapour deposition of vanadium diselenide thin films. *Appl. Surf. Sci.* **253,** 6041–6046 (2007).
68. Peters, E. S., Carmalt, C. J. & Parkin, I. P. Dual-source chemical vapour deposition of titanium sulfide thin films from tetrakisdimethylamidotitanium and sulfur precursors. *J. Mater. Chem.* **14,** 3474–3477 (2004).
69. Lauritsen, J. V. *et al.* Size-dependent structure of MoS_2 nanocrystals. *Nature Nanotech.* **2,** 53–58 (2007).
70. Tuxen, A. *et al.* Size threshold in the dibenzothiophene adsorption on MoS_2 nanoclusters. *ACS NANO* **4,** 4677–4682 (2010).
71. Lauritsen, J. V. Location and coordination of promoter atoms in Co- and Ni-Promoted MoS_2-based hydrotreating catalysts. *J. Catal.* **249,** 220–233 (2007).
72. Merki, D., Vrubel, H., Rovelli, L., Fierro, S. & Hu, X. Fe, Co, and Ni ions promote the catalytic activity of amorphous molybdenum sulfide films for hydrogen evolution. *Chem. Sci.* **2,** 2515–2525 (2012).
73. Greeley, J. *et al.* Computational high-throughput screening of electrocatalytic materials for hydrogen evolution. *Nature Mater*. **5,** 909–913 (2006).
74. Laursen, L. B., Kegnæs, S., Dahla, S. & Chorkendorff, I. Molybdenum sulfides efficient and viable materials for electro- and photoelectrocatalytic hydrogen evolution. *Energy Environ. Sci.* **5,** 5577–5591 (2012).
75. Li, Y. *et al.* MoS_2 nanoparticles grown on graphene: an advanced catalyst for the hydrogen evolution reaction. *J. Am. Chem. Soc.* **133,** 7296–7299 (2011).
76. Li, T. & Galli, G. Electronic properties of MoS_2 nanoparticles. *J. Phys. Chem. C* **111,** 16192–16196 (2007).
77. Merki, D. *et. al.* Amorphous molybdenum sulfide films as catalysts for electrochemical hydrogen production in water. *Chem. Sci.* **2,** 1262–1267 (2011).
78. Norskov, J. K. *et al.* Trends in the exchange current for hydrogen evolution. *J. Electrochem. Chem.* **152,** J23–J26 (2005).
79. Nørskov, J. K., Bligaard, T., Rossmeisl, J. & Christensen, C. H. Towards the computational design of solid catalysts. *Nature Chem.* **1,** 37–46 (2009).
80. Greeley, J. *et al.* Computational high-throughput screening of electrocatalytic materials for hydrogen evolution. *Nature Mater*. **5,** 909–913 (2006).
81. Bonde, J. *et al.* Hydrogen evolution on nano-particulate transition metal sulfides. *Faraday Discuss.* **140,** 219–231 (2008).
82. Jaramillo, T. F. *et al.* Identification of active edge sites for electrochemical H_2 evolution from MoS_2 nanocatalysts. *Science* **317,** 100–102 (2007).
83. Karunadasa, H. I. *et al.* A molecular MoS_2 edge site mimic for catalytic hydrogen generation, *Science* **335,** 698–702 (2012).
84. Chang, Y.-H. *et al.* Highly efficient electrocatalytic hydrogen production by MoS_x grown on graphene-protected 3D Ni foams. *Adv. Mater.* **25,** 756–760 (2013).
85. Wilcoxon, J. P. & Samara G. A. Strong quantum-size effects in a layered semiconductor: MoS_2 nanoclusters. *Phys. Rev. B* **51,** 7200 (1995).
86. Xiang, Q., Yu, J. & Jaroniec, M. Synergetic effect of MoS_2 and graphene as cocatalysts for enhanced photocatalytic H_2 production activity of TiO_2 nanoparticles. *J. Am. Chem. Soc.* **134,** 6575–6578 (2012).
87. Zhou, W. J. *et al.* Synthesis of few-layer MoS_2 nanosheet-coated TiO_2 nanobelt heterostructures for enhanced photocatalytic activities. *Small* **9,** 140–147 (2013).
88. Haering, R. R., Stiles, J. A. R. & Brandt, K. Lithium molybdenum disulphide battery cathode. US Patent 4224390 (1980).
89. Bhandavat, R., David, L. & Singh, G. Synthesis of surface-functionalized WS_2 nanosheets and performance as Li-ion battery anodes. *J. Phys. Chem. Lett.* **3,** 1523–1530 (2012).
90. Chang, K., Chen, W. L-Cysteine-assisted synthesis of layered MoS_2/graphene composites with excellent electrochemical properties for lithium ion batteries. *ACS Nano* **5,** 4720–4728 (2011).
91. Chang, K. & Chen, W. *In situ* synthesis of MoS_2/graphene nanosheet composites with extraordinarily high electrochemical performance for lithium ion batteries. *Chem. Commun.* **47,** 4252–4254 (2011).
92. Feng, C. Q. *et al.* Synthesis of molybdenum disulfide (MoS_2) for lithium ion battery applications. *Mater. Res. Bull.* **44,** 1811–1815 (2009).
93. Ding, S., Zhang, D., Chen, J. S. & Lou, X. W. Facile synthesis of hierarchical MoS_2 microspheres composed of few-layered nanosheets and their lithium storage properties. *Nanoscale* **4,** 95–98 (2012).
94. Zhang, C., Wang, Z., Guo, Z. & Lou, X. W. Synthesis of MoS_2-C one-dimensional nanostructures with improved Lithium storage properties. *ACS Appl. Mater. Interfaces* **4,** 3765–3768 (2012).
95. Ding, S., Chen, J. S. & Lou, X. W. Glucose-assisted growth of MoS_2 nanosheets on CNT backbone for improved Lithium storage properties. *Chem. Euro. J.* **17,** 13142–13145 (2011).
96. Zhang, C., Wu, H. B., Guo, Z. & Lou, X. W. Facile synthesis of carbon-coated MoS_2 nanorods with enhanced lithium storage properties. *Electrochem. Comm.* **20,** 7–10 (2012).
97. Chang, K. & Chen, W. L-Cysteine-assisted synthesis of layered MoS_2/graphene composites with excellent electrochemical performances for lithium ion batteries. *ACS Nano* **5,** 4720–4728 (2011).
98. Chang, K. & Chen, W. *In situ* synthesis of MoS_2/graphene nanosheet composites with extraordinarily high electrochemical performance for lithium ion batteries. *Chem. Comm.* **47,** 4252–4254 (2011).
99. Radisavljevic, B., Radenovic, A., Brivio, J., Giacometti, V. & Kis, A. Single-layer MoS_2 transistors. *Nature Nanotech.* **6,** 147–150 (2011).

© 2013 Macmillan Publishers Limited. All rights reserved

100. Radisavljevic, B., Whitwick, M. B. & Kis, A. Integrated circuits and logic operations based on single-layer MoS_2. *ACS Nano* **5,** 9934–9938 (2011).
101. Zhang, Y., Ye, J., Matsuhashi, Y. & Iwasa, Y. Ambipolar MoS_2 thin flake transistors. *Nano Lett.* **12,** 1136–1140 (2012).
102. Liu, L., Kumar, S. B., Ouyang, Y. & Gou, J. Performance limits of monolayer transition metal dichalcogenide transistors. *IEEE Trans. Electron Devices* **58,** 3042–3047 (2011).
103. Kaasbjerg, K., Thygesen, K. S. & Jacobsen, K. W. Phonon-limited mobility in n-type single-layer MoS_2 from first principles. *Phys. Rev. B* **85,** 115317 (2012).
104. Lee, K. *et al.* Electrical characteristics of molybdenum disulfide flakes produced by liquid exfoliation. *Adv. Mater.* **23,** 4178–4182 (2011).
105. Late, D. J., Liu, B., Matte, H. S. S. R., Dravid, V. P. & Rao, C. N. R. Hysteresis in single-layer MoS_2 field effect transistors. *ACS Nano* **6,** 5635–5641 (2012).
106. Fang, H. *et al.* High-performance single layered WSe_2 p-FETs with chemically doped contacts. *Nano Lett.* **12,** 3788–3792 (2012).
107. Wang, H. *et al.* Integrated circuits based on bilayer MoS_2 transistors. *Nano Lett.* **12,** 4674–4670 (2012).
108. Pu, J. *et al.* Highly flexible MoS_2 thin-film transistors with ion gel dielectrics. *Nano Lett.* **12,** 4013–4017 (2012).
109. Lee, S. H. *et al.* MoS_2 phototransistors with thickness-modulated optical energy gap. *Nano Lett.* **12,** 3695–3700 (2012).

Acknowledgements

M.C. acknowledges support from the National Science Foundation IGERT programme (DGE 0903661). H.Z. acknowledges support from the Singapore National Research Foundation under the CREATE programme: 'Nanomaterials for Energy and Water Management', and NTU under the Start-Up Grant M4080865.070.706022. H.S.S. acknowledges support from WCU (World Class University) programme (R31-2008-000-20012-0) and the grant (Code No. 2011-0031630) from the Center for Advanced Soft Electronics under the Global Frontier Research Program through the National Research Foundation funded by MEST of Korea. G.E. acknowledges the Singapore National Research Foundation for NRF Research Fellowship (NRF-NRFF2011-02). L.L. acknowledges support from Academia Sinica Taiwan. We acknowledge Jieun Yang for editorial help and TOC artwork. K.P.L. acknowledges the NRF-CRP award 'Novel 2D materials with tailored properties: beyond graphene' (R-144-000-295-281).

Additional information

Reprints and permissions information is available online at www.nature.com/reprints. Correspondence should be addressed to M. C.

Competing financial interests

The authors declare no competing financial interests.

© 2013 Macmillan Publishers Limited. All rights reserved